Nanoscale

Visualizing Charges Accumulated in Electric Double Layer by Three-Dimensional Open-Loop Electric Potential Microscopy

Journal:	*Nanoscale*
Manuscript ID	NR-ART-05-2018-003600.R1
Article Type:	Paper
Date Submitted by the Author:	29-Jun-2018
Complete List of Authors:	Hirata, Kaito; Kanazawa University Kitagawa, Takuya; Kanazawa University Miyazawa, Keisuke; Kanazawa University, Okamoto, Takahiro; Kanazawa University Fukunaga, Akira; Ebara Corporation Takatoh, Chikako; Ebara Corporation Fukuma, Takeshi; Kanazawa University,

Journal Name

ARTICLE TYPE

Cite this: DOI: 10.1039/xxxxxxxxxx

Visualizing Charges Accumulated in Electric Double Layer by Three-Dimensional Open-Loop Electric Potential Microscopy†

Kaito Hirata,[a] Takuya Kitagawa,[a] Keisuke Miyazawa,[a] Takahiro Okamoto,[a] Akira Fukunaga,[b] Chikako Takatoh,[b] and Takeshi Fukuma*[a,c]

Received Date
Accepted Date

DOI: 10.1039/xxxxxxxxxx

www.rsc.org/journalname

Charges accumulated in an electric double layer (EDL) play key roles in various interfacial phenomena and electronic devices. However, direct imaging of their spatial distribution has been a great challenge, which has hindered our nano-level understanding on the mechanisms of such interfacial phenomena and functions. In this study, we present direct imaging of charges accumulated at an electrode-electrolyte interface using three-dimensional open-loop electric potential microscopy (3D-OL-EPM). Conventional OL-EPM allows us to visualize two-dimensional potential distributions in liquid yet the zero of the measured potential is not well defined due to the influence of the long-range (LR) interaction between the cantilever and the sample. Here, we present practical ways to reduce such influence by improving the equation for the potential calculation and subtracting the LR contribution estimated from a Z potential profile. These improvements enabled to calibrate the measured potential values with respect to the bulk solution potential. With these improvements, we visualized opposite charge accumulation behaviors on a polarizable and non-polarizable electrode with varying electrode potential. Combining OL-EPM with a 3D tip scanning method, we also performed a 3D-OL-EPM measurement on a Cu fine wire and visualized nanoscale distribution of the charges accumulated at the interface. Such real-space information on the charge distributions in an EDL should provide valuable insights into the mechanisms of interfacial phenomena and functions that are important in various academic and industrial research on electronic devices, electrochemistry, tribology and life sciences.

1 Introduction

Electric double layer (EDL) formed at an electrode-electrolyte interface gives significant influence on the interaction between the electrode and adjacent species such as water[1,2], ions[3–5] and molecules[6,7]. This can alter the functions of various devices such as EDL capacitors[8–11], transistors[12,13], superconductors[14] and spintronic devices[15], and various phenomena such as corrosion[6,7,16] and molecular and cellular adhesions[17,18]. To understand the mechanisms of these functions and phenomena, the charge distribution within an EDL have widely been studied from theoretical and experimental aspects[19–21].

From the experimental point of view, this has been a great challenge. Since an EDL has nanoscale vertical and lateral distribution, detailed understanding of the EDL properties requires three-dimensional (3D) nanoscale measurements of charge distribution at a solid-liquid interface. While widely used methods such as impedance spectroscopy[7,11], dynamic light scattering[22] and surface force apparatus measurements[17] provide nanoscale information on the vertical distribution of an EDL, direct measurements of its lateral distribution has been very challenging.

Atomic force microscopy (AFM)[23] is one of the most promising methods that may allow us to solve this problem. The existing AFM-based potential measurement techniques can be classified into two categories: the force curve method[24,25] and the bias modulation method[26–28]. In the former case, a force versus distance curve is measured on an electrode and the theoretical equation is fitted to the curve to determine the local surface charge density. One of the major advantages of this method is its capability of discriminating the short-range (SR) force acting on the tip apex from the long-range (LR) force acting on the other parts of a cantilever and a tip to a certain extent. However, it is difficult to discriminate the electrostatic force from the other forces such as hydration or fluctuation-induced forces[17] unless multiple mea-

[a] Division of Electrical Engineering and Computer Science, Kanazawa University, Kakuma-machi, 920-1192 Kanazawa, Japan, Fax: +81-76-234-4632; Tel: +81-76-234-4847; E-mail: fukuma@staff.kanazawa-u.ac.jp
[b] EBARA Corporation, 144-8510 Tokyo, Japan
[c] Nano Life Science Institute (WPI-NanoLSI), Kanazawa University, Kakuma-machi, 920-1192 Kanazawa, Japan

surements are performed with varying solution conditions. This drawback can significantly limit the application range of this type of methods.

In the bias modulation method, an ac bias voltage is applied between a tip and an electrode and the induced electrostatic force is measured to determine the local surface potential. Thus, the electrostatic force is discriminated from the other forces. Among various implementations of the bias modulation method, Kelvin probe force microscopy (KPFM)[26] is the most widely used technique for applications in air or vacuum. However, recent studies from several groups showed that the method cannot be used in an electrolyte stably or accurately. This is mainly because KPFM requires application of a dc bias voltage, which induces uncontrolled electrochemical reactions and redistribution of water and ions[27–29].

To overcome this limitation, we have recently developed open-loop electric potential microscopy (OL-EPM)[27,30,31]. In OL-EPM, only an ac bias voltage with a relatively high frequency is applied between a tip and a sample so that we can avoid the aforementioned problems in KPFM. The first and second harmonic oscillations of a cantilever induced by the bias application are detected and used for calculating local surface potential. While OL-EPM allows us to selectively detect the bias-induced electrostatic force, it does not allow us to discriminate forces with different interaction ranges. Thus, there have been debates on the locality and accuracy of the potential measured by OL-EPM[28,32–34].

Recently, the question on the locality was positively answered by the direct visualization of nanoscale distribution of local corrosion cells during the corrosion of copper fine wires and stainless steel in an electrolyte[35]. In these experiments, the nanoscale distribution of corrosion sites (i.e. anodic areas) were visualized with a higher potential than the other areas (i.e. cathodic areas). This result demonstrated that the SR electrostatic force can predominantly contribute to the formation of nanoscale contrasts in a potential image. However, there still remains a room for improving its locality and accuracy by reducing the contributions from the LR force.

In general, anodic and cathodic reactions respectively increase the relative cation and anion densities in the solution near the electrode surface. This is consistent with the results of the previous imaging of corrosion sites[35], where the anodic and cathodic areas were respectively visualized with a higher and lower potential contrast. This agreement suggests that the potential distribution measured by OL-EPM represents local charge distribution in an EDL. However, such a possibility has not been confirmed by systematic experiments.

In this study, we have investigated the possibility of imaging accumulated charges in an EDL by OL-EPM. First, we present practical methods for reducing the contribution from the LR force to the potential measured by OL-EPM. Based on these improvements, we visualize accumulated charges in an ELD formed on a polarizable and a non-polarizable electrode with varying electrochemical potential. Finally, we combine OL-EPM with a 3D scanning technique to visualize nanoscale distribution of EDL on a Cu fine wire in electrolyte.

2 Methods

2.1 OL-EPM measurements

In this study, we used a custom-built AFM instrument with an ultralow noise cantilever deflection sensor[36,37] and a highly stable photothermal cantilever excitation system[38,39]. The tip–sample distance was regulated such that the cantilever oscillation amplitude was kept constant. A commercially available AFM controller (RC4/OC4, SPECS) was used for the OL-EPM operation. Si cantilevers (AC55, Olympus) having a nominal spring constant of ~85 N/m, a typical resonance frequency of ~1 MHz and a Q factor of ~10 in an aqueous solution were used. These cantilevers come with a Au backside coating. In addition, we coated their front side with a 30 nm Au film using a dc sputter coater (K575XD, Emitech). The typical tip radius after the Au coating was approximately 20 nm. An ac bias voltage was produced by adding a sine wave $V_{ac}\cos\omega_2 t$ from a function generator (AFG3022B, Tektronix) to another sine wave $V_{ac}\cos\omega_1 t$ from a lock-in amplifier (HF2LI: Zurich Instruments). The amplitudes of the ω_1 and $\omega_L(=|\omega_2-\omega_1|)$ components (A_1 and A_L), and the phase of the ω_1 component (ϕ_1) were detected from a cantilever deflection signal using the same lock-in amplifier. All the OL-EPM measurements were performed at room temperature in the dual frequency (DF) mode. The imaging parameters such as V_{ac}, $f_1(=\omega_1/2\pi)$ and $f_2(=\omega_2/2\pi)$ are given in the figure captions. For the electrochemical OL-EPM (EC-OL-EPM) setup (Figure 4), we used a commercially available potentiostat (HZ-5000, Hokuto Denko).

2.2 Preparation of the Cu fine wire samples

We used patterned Cu fine wires fabricated on a Si wafer (854 Cu CMPd Wafer, Advanced Materials Technology) for the experiments shown in Figure 8. The Cu wires were formed on a 25 nm Ta film and had a thickness of 475 nm. An outline of the fabrication process is as follows. (1) Patterned trench structures were formed by etching the SiO_2 layer on the Si wafer. (2) A 25 nm Ta film was formed on the wafer surface by physical vapor deposition. (3) A thick Cu film was formed on the Ta film by electroplating. (4) The wafer was annealed at 150°C for 30 min. (5) The surface was polished by chemical mechanical polishing machine to reduce the SiO_2 thickness to 500 nm, which corresponds to a Cu wire thickness of 475 nm. In this way, polycrystalline Cu fine wires were fabricated. The wires consist of nanoscale grains with different crystallographic orientations. For the AFM measurements, we cut the wafer into pieces with a size of 10 mm × 10 mm.

To remove surface contaminants, we cleaned the surface using an Ar plasma cleaner (SC-701, Sanyu Electronics). We found that the Ar plasma cleaning under typical operating conditions can severely damage the Cu wires. Thus, we adjusted the bias voltage and inlet gas pressure to the minimum values required to maintain the plasma. In addition, we covered the sample with a Cu plate to suppress the electric field applied to the sample surface. Under these conditions, the damage of the wires caused by the cleaning was negligible.

After the Ar plasma cleaning, we attached the sample to a sam-

ple holder for our AFM system. On the fixed sample, we added dropwise 100 μL 0.5 M citric acid solution and left the sample for 1 min to remove organic contaminants deposited on the surface during the sample transfer process. Subsequently, we exchanged the deposited solution with pure water by gentle pipetting. We repeated this process five times not only to completely replace the solution but also to rinse the surface with pure water.

We set the sample holder onto our AFM system. Immediately before starting the coarse approach of the tip, we replaced the water on the sample with an imaging solution, i.e., 0.1 mM NaCl solution. We repeated this process twice to completely replace the solution with the imaging solution.

2.3 Preparation of Au, Pt and Cu thin films

We used Au, Pt and Cu thin films for the experiments shown in Figures 2, 3, 6 and 7. The Au and Pt thin films were prepared as follows. Round-shaped muscovite mica substrates with a diameter of 12 mm (01877-MB, SPI Supplies) were cleaved in air. Immediately after the cleavage, we introduced the sample into the vacuum chamber of the sputter coater (K575XD, Emitech). We deposited a 5 nm Ti film as an adhesion layer and a 100 nm Au or Pt thin film on it. After taking out the sample from the vacuum chamber, we dropped a 100 μL of 0.1 mM or 1 mM solution and performed OL-EPM measurements in the solution.

As for the Cu thin films, we used a commercially available electroplated Cu thin film formed on a Si substrate. Before the OL-EPM measurements, the surface was cleaned by the Ar plasma cleaning and the citric acid treatment. The detailed procedures are the same as those used for the Cu fine wires.

3 Results and Discussion

3.1 Basic Principle of OL-EPM

The details of the principle and setup for OL-EPM were reported previously[27,30,31]. Thus, here we only describe their short summary. So far, there have been reported two different operation modes: the single frequency (SF)[27] and the dual frequency (DF)[31] modes. In the following discussions, we will mostly assume the SF mode as similar discussions are also applicable to the DF mode. However, some of the important equations will be described for each mode.

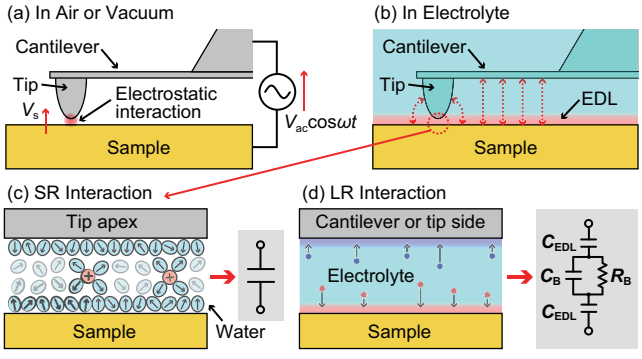

Fig. 1 Basic principle of OL-EPM (a) in air or vacuum, and (b) in electrolyte. Simplified models of the (c) SR and (d) LR interactions.

In OL-EPM, an ac bias voltage $V_{ac}\cos\omega t$ is applied between the tip and the sample (Figure 1a). In air or vacuum, the electric field is mostly focused on the tip apex. Thus, the LR force acting on the tip sidewall and cantilever (F_ℓ) is often much smaller than the SR force acting on the tip apex (F_s). If we define V_s as the local surface potential with respect to the macroscopic sample potential, F_s is described by[26]

$$F_s = \frac{1}{2}\frac{\partial C_s}{\partial z}\left[V_s^2 + \frac{1}{2}V_{ac}^2 - 2V_{ac}V_s\cos(\omega t) + \frac{1}{2}V_{ac}^2\cos(2\omega t)\right], \quad (1)$$

where C_s and z denote the local capacitance and the distance between the tip apex and the sample surface. This equation shows that F_s contains dc, ω and 2ω components. These components respectively induce cantilever deflections. The amplitudes of the cantilever oscillations at ω and 2ω are respectively described by

$$A_1 = \left|\frac{\partial C_s}{\partial z}V_s\right| V_{ac}G(\omega), \quad (2)$$

$$A_2 = \left|\frac{\partial C_s}{\partial z}\right| \frac{V_{ac}^2}{4}G(2\omega), \quad (3)$$

where $G(\omega)$ denotes the transfer function from the force applied to the tip to the cantilever deflection at ω. These equations show that $|\partial C_s/\partial z|$ can be eliminated by taking a ratio between A_1 and A_2. Thus, V_s can be calculated by the following equation.

$$V_s = \mathrm{sgn}(\cos\phi_1)\frac{A_1/G(\omega)}{A_2/G(2\omega)}\frac{V_{ac}}{4}, \quad (4)$$

where ϕ_1 denotes the phase of the cantilever vibration at ω with respect to the ac bias voltage signal.

In the DF mode[31], the sum of two ac bias voltages with different frequencies (ω_1 and ω_2) are applied between the tip and the sample. Then, the amplitudes (A_1 and A_L) of the induced cantilever vibrations at ω_1 and $\omega_L(\equiv|\omega_1-\omega_2|)$ are detected. From these parameters, V_s is calculated by the following equation:

$$V_s = \mathrm{sgn}(\cos\phi_1)\frac{A_1/G(\omega_1)}{A_L/G(\omega_L)}\frac{V_{ac}}{2}. \quad (5)$$

Ideally, $\cos\phi_1$ should take 1 or -1 so that the $\mathrm{sgn}(\cos\phi_1)$ can be replaced by $\cos\phi_1$. In practice, there are finite phase noise and delay so that we proposed to use $\mathrm{sgn}(\cos\phi_1)$ to eliminate their influence on the calculated V_s[27]. However, we subsequently found that this was not necessarily the best choice for the measurements in electrolyte because of the contribution from F_ℓ having a large phase delay. This issue will be further discussed in the following section.

3.2 Bias-Induced Forces in Electrolyte

In electrolyte, the tip and the cantilever are surrounded by aqueous solution with a high dielectric constant ($\simeq 80$). Thus, the contribution from F_ℓ becomes more evident (Figure 1b) than that in air or vacuum. In addition, the bias application induces various processes with different timescales[28]. The timescales of the electrochemical reactions and the surface diffusion of adsorbates are on the order of milliseconds, which is much slower than that

of the bias modulation (1–2 μs) and hence negligible.

In contrast, the timescale of the charge diffusion within an EDL is on the order of nanoseconds, which is much faster than the timescale of the bias modulation. Thus, the medium within an EDL should behave as a simple dielectric material to the applied ac electric field. Since the tip-sample distance ($<$ 1 nm) during an OL-EPM measurement is typically shorter than the thickness of an EDL, the tip-sample junction should behave as a capacitor as shown in Figure 1c. Hence, Equation (1) should be valid at least for the SR force F_s. The main difference from vacuum-environment experiments is that net charges exist within the tip-sample junction (Figure 1c), which produce an extra dc electric field applied to the tip apex and hence influence V_s.

The timescale of the charging and discharging of the diffuse layer through the ion diffusion in the bulk solution is comparable to the timescale of the bias modulation (0.1–10 μs). This behavior can be modeled by the simplified equivalent circuit shown in Figure 1d[33]. In this figure, the capacitance at the EDL (C_{EDL}) is charged or discharged through the resistance of the bulk solution (R_B) with a time constant of $C_{EDL}R_B$. Thus, F_ℓ often shows a significant phase delay and does not follow the behavior expected from Equation (1).

The SR interaction at the tip-sample junction ideally produces only an in-phase component in F_s with respect to the bias voltage signal. However, the LR interaction produces in-phase and quadratic-phase components in F_ℓ. Thus, the ω and 2ω components (F_1 and F_2) of the total electrostatic force are given by

$$F_1 = F_{s1}\cos(\omega t) + F^{i}_{\ell 1}\cos(\omega t) + F^{q}_{\ell 1}\sin(\omega t), \quad (6)$$

$$F_2 = F_{s2}\cos(2\omega t) + F^{i}_{\ell 2}\cos(2\omega t) + F^{q}_{\ell 2}\sin(2\omega t), \quad (7)$$

where $F_{s1}, F_{s2}, F^{i}_{\ell 1}, F^{i}_{\ell 2}, F^{q}_{\ell 1}$ and $F^{q}_{\ell 2}$ are the amplitudes of the individual force components. The subscripts 1 and 2 denote the ω and 2ω components while s and ℓ denote the SR and LR interactions, respectively. The superscripts i and q denote the in-phase and quadratic-phase components, respectively. Among these six components, the four components originating from the LR interaction lead to an error in the potential measurements. Although it is difficult to fully eliminate the influence of these components, we discuss practical methods for reducing it in the following section.

3.3 Practical Methods for Reducing the Influence of F_ℓ

3.3.1 Eliminating the contribution from $F^{q}_{\ell 1}$

Among the four error components in Equations (6) and (7), the in-phase components cannot be easily eliminated from the $F_{\ell 1}$ or $F_{\ell 2}$. However, the quadratic-components can be eliminated by multiplying A_1 and A_2 respectively by $\cos\phi_1$ and $\cos\phi_2$, where ϕ_2 denotes the phase of the 2ω-component of the cantilever oscillation with respect to the bias voltage signal. Thus, Equation (4) can be improved as follows.

$$V_s = \frac{A_1\cos\phi_1/G(\omega)}{A_2\cos\phi_2/G(2\omega)}\frac{V_{ac}}{4}. \quad (8)$$

In practice, the experimentally measured ϕ_2 signal often contains relatively large noise. Thus, the $\cos\phi_2$ signal can take a value close to zero, leading to an extremely large value of V_s. Although this problem may be solved by the future improvement in the force sensitivity, we propose to use the following equation as the current practical solution.

$$V_s = \frac{A_1\cos\phi_1/G(\omega)}{A_2/G(2\omega)}\frac{V_{ac}}{4}. \quad (9)$$

For the DF mode, this equation is described by

$$V_s = \frac{A_1\cos\phi_1/G(\omega)}{A_L/G(2\omega_L)}\frac{V_{ac}}{2}. \quad (10)$$

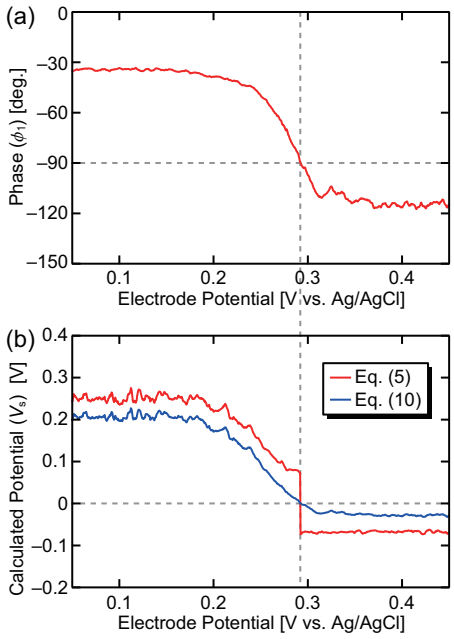

Fig. 2 (a) ϕ_1 and (b) V_s versus E curves measured on the Au electrode in 0.1 mM NaCl solution. Cantilever resonance frequency (f_0) was 1.4 MHz. $f_1 = 700$ kHz. $f_2 = 730$ kHz. $V_{ac} = 0.8$ V.

The use of Equations (9) and (10) instead of Equations (4) and (5) eliminates the influence of $F^{q}_{\ell 1}$. This improvement gives a dramatic effect when V_s is close to zero. An example of such measurements is shown in Figure 2. In this experiment, the electrochemical potential (E) of a Au electrode was varied with respect to the Ag/AgCl reference electrode in 0.1 mM NaCl solution and the induced variations in ϕ_1 and V_s were recorded. While the mechanisms of the E dependence of ϕ_1 and V_s will be discussed later, here we focus on the difference between the V_s curves obtained by Equations (5) and (10).

Figure 2a shows that ϕ_1 is not necessarily close to 0° or 180° but can take an intermediate value. This result shows that the contribution from $F^{q}_{\ell 1}$ is not negligible. In fact, Figure 2b shows the clear difference between the V_s curves obtained by Equations (5) and (10). The curve obtained by Equation (5) shows a discontinuous jump at −0.29 V, which is an artifact caused by $F^{q}_{\ell 1}$. In the meanwhile, the curve obtained by Equation (10) shows a smooth profile, demonstrating the importance of eliminating the contribution from $F^{q}_{\ell 1}$.

3.3.2 Reducing the Influence from F_ℓ

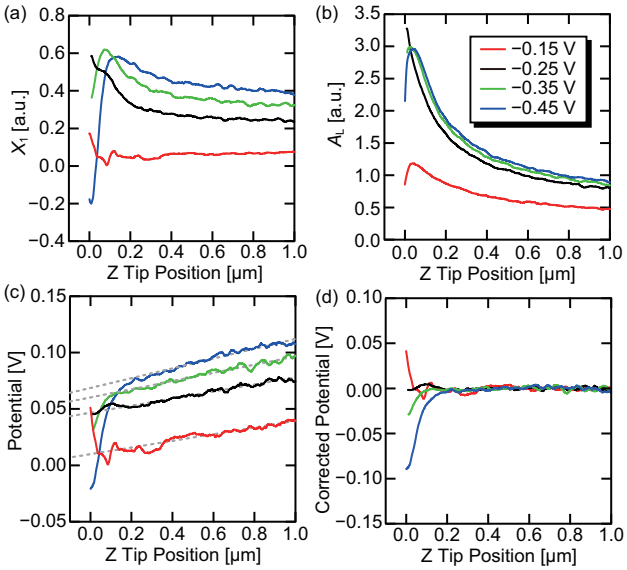

Fig. 3 Z dependence of (a) X_1, (b) A_L, (c) V_s calculated by Equation (10), and (d) SR components of V_s extracted from (c). The measurements were performed on the Cu electrode in 0.1 mM NaCl solution with different E with respect to the Ag/AgCl reference electrode. The dotted lines in (c) represent the estimated LR components of V_s. $f_0 = 1.15$ MHz. $f_1 = 700$ kHz. $f_2 = 730$ kHz. $V_{ac} = 0.8$ V.

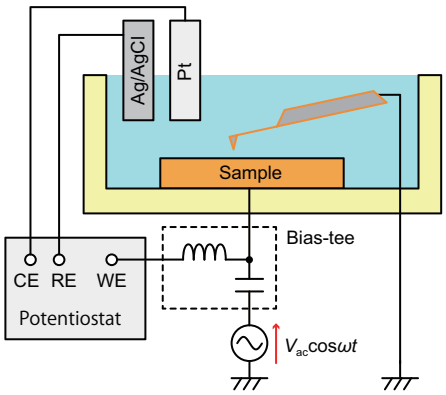

Fig. 4 Experimental setup for OL-EPM measurements with an electrochemical control system.

By measuring the Z dependence of $A_1 \cos\phi_1 (\equiv X_1)$ and A_L, the contribution from F_ℓ to the calculated V_s value can be estimated to a certain extent. An example of such measurements is shown in Figure 3. We measured Z dependence of X_1 and A_L on the Cu electrode in 0.1 mM NaCl solution with different E with respect to the Ag/AgCl reference electrode (Figures 3a and 3b). For this measurement, we used an OL-EPM setup with an electrochemical control system (EC-OL-EPM) as shown in Figure 4. From the obtained X_1 and A_L curves, the V_s curves were calculated using Equation (10) as shown in Figure 3c.

Ideally, we should estimate the LR components of F_1 and F_2 and subtract them respectively from their originals. However, an F_2 signal practically has relatively large noise so that the F_2 values after the subtraction can take nearly zero or negative values. As the calculation of the potential involves a division by A_2, which is proportional to F_2, the influence of the noise is extremely enhanced. Thus, this method cannot be practically useful at least with the current force detection limit. As a practical solution, here we propose to calculate V_s curve by Equation (9) or (10) and subtract its linear fit to reduce the influence from F_ℓ. While there have been several attempts to analytically describe the F_1 or F_2 curves[25,32] all of them have significant limitations in their practical use. In the meanwhile, we found that experimentally obtained V_s curves always show a linear Z dependence at far away from the surface as shown in Figure 3c. Therefore, we empirically decided to use a linear function to model the LR part of a Z potential profile.

The effectiveness of the proposed method is well demonstrated by the examples shown in Figure 3. The dotted lines in Figure 3c show the fitted curves while the SR components after the LR subtraction are shown in Figure 3d. These SR potential curves show that V_s at the closest tip position to the surface monotonically increases with increasing E. This E dependence was not evident before the LR subtraction. These results demonstrate the importance of the LR subtraction for investigating the interfacial charges accumulated in the EDL. For example, at E of -0.45 V and -0.15 V, the V_s curves show a sharp decrease and increase near the surface, suggesting the accumulation of negative and positive charges in the EDL, respectively.

Here, we should note the difference between this experiment and an OL-EPM imaging. In this experiment, we varied the global E so that the LR force is significantly changed. In contrast, in an OL-EPM imaging, we typically scan a tip locally in an area much smaller than the cantilever dimension. Thus, the LR force is almost constant during the imaging and the observed potential contrasts mainly reflect the local potential distribution. However, the potential values recorded during the tip scan is almost equally influenced by the LR force. For eliminating such influence and estimating the quantitative potential value with respect to that in the bulk solution, we should at least measure one V_s versus distance curve at a location in the scan area.

3.4 Visualizing Charges Accumulated in an EDL

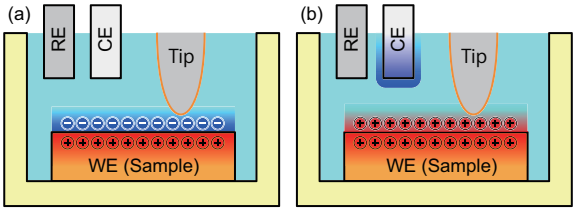

Fig. 5 Charge accumulation in an EDL on a polarizable and a non-polarizable electrode with anodic E. (a) Polarizable electrode such as Au and Pt. (b) Non-polarizable electrode such as Cu.

To confirm the capability of OL-EPM to visualize charges accumulated in an EDL, here we use polarizable and non-polarizable

electrodes (Figure 5). These two types of electrodes show different charge accumulation behaviors at the interface with electrolyte as shown in Figure 5. When we control E to an anodic value using the EC-OL-EPM setup shown in Figure 4, positive charges are supplied from a potentiostat to the electrode. For a polarizable electrode, these positive charges are mainly accumulated just under the surface and they are electrostatically screened by the reorientation of polar molecules (e.g., water) or accumulation of anions (Figure 5a). This forms an EDL with negative charges accumulated in the solution near the surface. In contrast, on a non-polarizable electrode, positive charges are mainly transferred into the solution through oxidative reactions (Figure 5b). This leads to an increase of positive charges at the electrode-electrolyte interface. Therefore, these two electrodes show opposite dependence on E.

In this study, the Au and Pt thin films were used as a polarizable electrode while the Cu thin film was used as a non-polarizable electrode. We measured Z profiles of the OL-EPM potential with varying E to obtain two-dimensional (2D) potential maps as shown in Figure 6(i). These 2D maps visualize strong dependence of the OL-EPM potential on both E and Z. For the polarizable electrodes (i.e., Au and Pt), the Z potential profiles show a sharp increase at a lower E while a decrease at a higher E. In contrast, the non-polarizable electrode (i.e. Cu) shows an opposite behavior.

Figure 6(ii) shows lateral cross-sectional profiles of these 2D maps at the closest tip position to the surface. These profiles show E dependence of the "local" surface potential originating from the local charges and dipoles at the solid-liquid interface. As for the contribution from the global electric field in a dilute solution, it is largely eliminated by the LR subtraction process. The local surface potential at the solid-liquid interface depends on various factors such as local surface structures, and arrangements of ions, water and other adsorbates. Thus, it is difficult to accurately compare the results obtained by different experiments. However, we found that the range of the local surface potential measured in our experiments is comparable to the previously reported one. For example, the previous studies by AFM force-curve measurements[40–45] suggest that the surface potential of gold in neutral solutions of low salt concentration vary from -70 mV to $+130$ mV. This potential variation approximately agrees with that observed in our experiments (-90 mV to $+110$ mV) as shown in Figures 6 and 7.

For the polarizable electrodes, the local surface potential decreases with increasing E. In contrast, the polarizable electrode shows an opposite E dependence. These different behaviors are particularly evident around the zero-cross point, where the local surface potential shows a linear dependence on E. E for the zero-cross point (E_z) increases in the order of Cu (-430 mV) $<$ Pt (185 mV) $<$ Au (345 mV).

The macroscopic electrode current (I) during these measurements was also recorded as shown in Figure 6(iii). Overall, the current increases in the order of Au $<$ Pt $<$ Cu. The spontaneous potential (E_s) increases in the order of Cu $<$ Pt $<$ Au. These results are consistent with the general understandings in electrochemistry.

Figure 6(iv) shows typical Z profiles extracted from the 2D maps at a high, intermediate and low E. Among them, the intermediate E corresponds to E_z. These E values are indicated by the dotted lines and triangular markers in the 2D maps (Figure 6(i)). The potential profiles obtained at E_z shows almost no dependence on the Z tip position. This result shows that the local electric field around the tip apex did not change during the tip approach. Thus, the local surface potential should be the same as that of the bulk solution. Similarly, the increase or decrease observed in the potential profiles near the surface indicates the positive or negative potentials with respect to the bulk solution, respectively.

The Z profiles shown in Figure 6 reveal that the non-linear potential change appears only in the Z range (Δz) less than 300 nm from the surface. To investigate the correlation between Δz and ion concentration (C_{ion}), we performed similar measurements in 0.1 mM and 1 mM NaCl solution on a Au electrode as shown in Figure 7. The results obtained under these two conditions are mostly the same. However, Δz in 0.1 mM is significantly larger than that in 1 mM. We estimated the decay length (λ_p) of the typical potential profiles by fitting an exponential function ($A\exp(-z/\lambda_p)+y_0$) to the curves shown in Figure 7(iv). The average λ_p in 0.1 mM and 1 mM solutions are 98 nm and 35 nm, respectively. The obtained values of λ_p suggest that the EDL depth in 0.1 mM is three times larger than that in 1 mM. This is consistent with the C_{ion} dependence of the Debye length (λ_D): $\lambda_D \propto 1/\sqrt{C}$.

In general, λ_D is often used as an estimate of the EDL depth. λ_D is defined as a decay length of charge density distribution at a solid-liquid interface. Thus, it can be directly compared with λ_p. For 0.1 mM and 1 mM NaCl solutions, λ_D is 30 nm and 9.6 nm, respectively. These values are three times smaller than those of λ_p for both the solution conditions. As one of the possible explanations to this difference, we tentatively suggest that the remaining contribution from the LR interaction may result in an increase of the decay length.

Equations (9) and (10) were derived by assuming that the local tip-sample junction is in an EDL. Thus, the potential values in the 2D maps especially at a Z tip position higher than λ_D may not be accurate. Therefore, at this stage, it is reasonable to use the 2D maps only for the discussions on the vertical extent of an EDL while the quantitative discussions should be made only based on the local surface potential profiles (e.g. Figures 6(ii) and 7(ii)).

In summary, the observed E dependence of the Z potential profiles is consistent with the expected charge accumulation behaviors of polarizable and non-polarizable electrodes. This result confirms the capability of OL-EPM to visualize charges accumulated at an electrode-electrolyte interface. The apparent EDL depth observed in the 2D maps is proportional to the true EDL but three-times overestimated under our experimental conditions. The generality of this relationship should be confirmed by more systematic studies with different types of electrodes in the future.

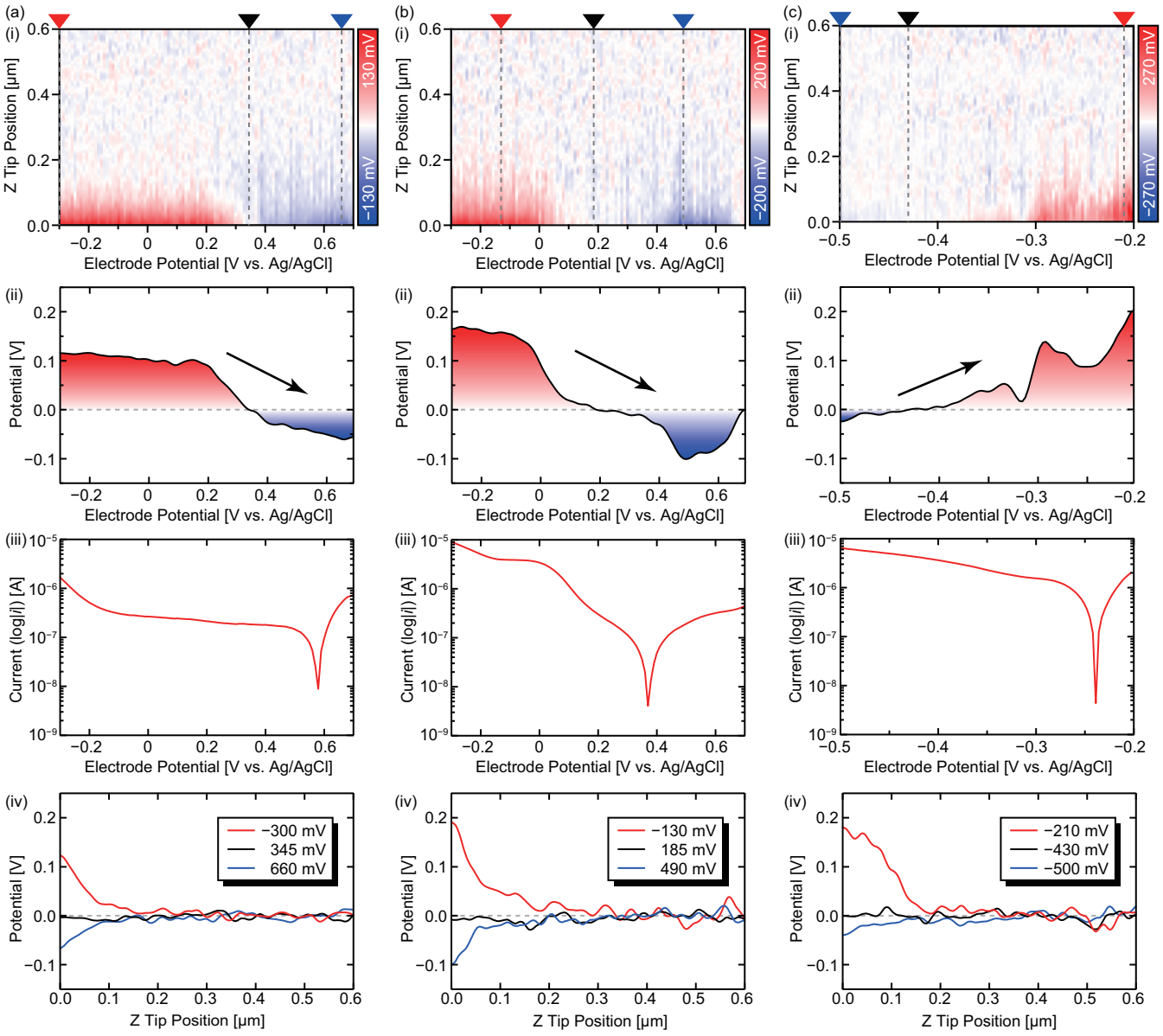

Fig. 6 Z potential profiles measured with varying E in 0.1 mM NaCl solution on a polarizable ((a) Au and (b) Pt) and non-polarizable ((c) Cu) electrode. (i) 2D maps showing the dependence of the measured potential after the LR subtraction on E and Z. (ii) Lateral cross-sectional profiles of the 2D maps shown in (a) taken at the closest tip position to the surface. (iii) Dependence of I on E during the measurements. (iv) Z cross-sectional profiles of the 2D maps shown in (a) taken at a high, intermediate and low E. $f_0 = 1.3$–1.5 MHz. $f_1 = 700$ kHz. $f_2 = 730$ kHz. $V_{ac} = 0.8$ V.

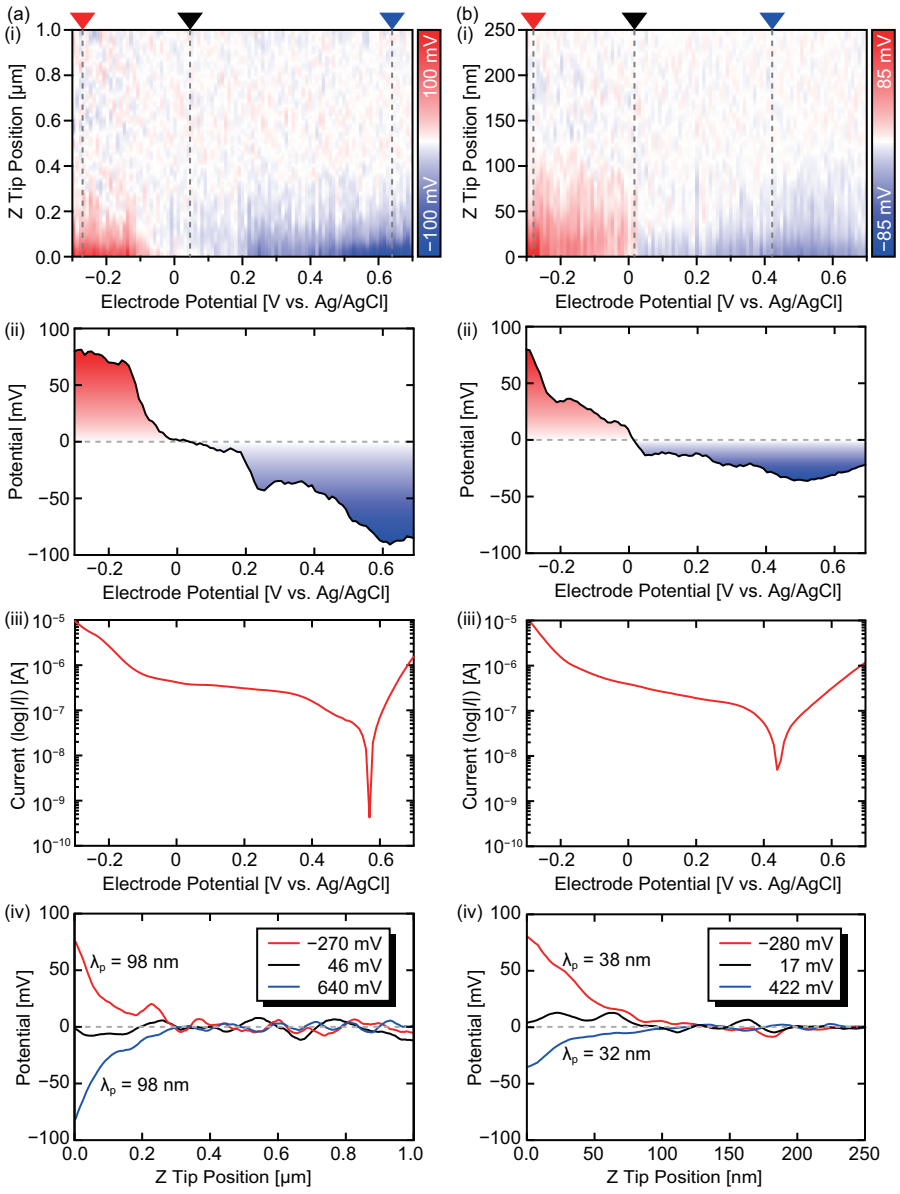

Fig. 7 Z potential profiles measured with varying E in 0.1 mM and 1 mM NaCl solution on the Au electrode. (i) 2D maps showing the dependence of the measured potential after the LR subtraction on E and Z. (ii) Lateral cross-sectional profiles of the 2D maps shown in (a) taken at the closest tip position to the surface. (iii) Dependence of I on E during the measurements. (iv) Z cross-sectional profiles of the 2D maps shown in (a) taken at a high, intermediate and low E. $f_0 = 1.1$–1.2 MHz. $f_1 = 700$ kHz. $f_2 = 730$ kHz. $V_{ac} = 0.8$ V.

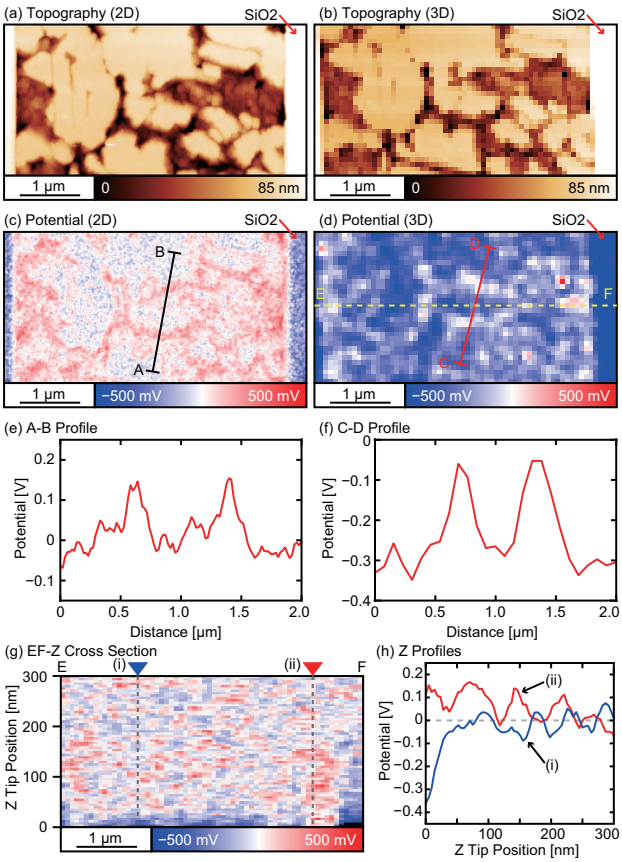

Fig. 8 2D and 3D OL-EPM measurements of Cu fine wires in 0.1 mM NaCl solution. (a) Topographic and (c) potential images obtained by 2D-OL-EPM (256 × 128 pix^2, 3 min/frame). (b) Topographic and (d) potential images obtained by 3D-OL-EPM (64 × 32 × 256 pix^3, 10 min/volume). Potential profiles taken along (e) line A–B and (f) line C–D. (g) Z cross section taken along line E–F. (h) Z profiles taken at the positions indicated by the dotted lines shown in (g). $f_0 = 965$ kHz. $f_1 = 700$ kHz. $f_2 = 730$ kHz. $V_{ac} = 0.8$ V.

3.5 3D-OL-EPM Measurements of Cu Fine Wires

By taking Z potential profiles at arrayed XY positions and subtracting the LR contribution from them, we can produce a 3D potential map and a 2D local surface potential image. To investigate such a possibility, we performed 2D and 3D OL-EPM measurements of Cu fine wires in 0.1 mM solution as shown in Figure 8. The topographic images obtained by the two methods show similar contrasts although the pixel resolutions are different. The brighter regions at the left and right edges correspond to the insulator (SiO_2) while the area at the center corresponds to the Cu fine wire. The grains constituting the Cu fine wire show different corrosion resistance due to the different crystallographic orientations[46]. In the topographic images, the flat terraces and the depressed areas correspond to the grains having a relatively high and low corrosion resistance, respectively.

The potential image obtained by 2D-OL-EPM (Figure 8c) shows that the depressed areas has a higher potential and hence a higher corrosion activity than the flat terraces. In this way, 2D-OL-EPM allows us to visualize the distribution of the relative corrosion activities. However, it does not allow us to discuss absolute corrosion activity due to the uncertainty of the zero potential.

This problem is solved by 3D-OL-EPM. Figure 8d shows an XY cross section of the 3D potential map obtained at the closest tip position to the surface. This 2D image shows lateral distribution of the local surface potential with respect to the bulk solution potential. The observed nanoscale contrasts largely agree with those found in the 2D-OL-EPM image. In addition, comparison between the potential profiles along lines A–B and C–D reveal that the relative potential distributions observed by the two methods are similar. However, their absolute value is different by ∼250 mV. To highlight this difference, we displayed the two images with the same color scale.

In general, a cross talk between the topographic and potential images can be a serious problem in an AFM measurement of surface property distribution. However, for this particular system, we have reasons to believe that the influence from such a cross talk is minor. So far, we have performed many 2D-OL-EPM measurements of the same system with the same type of tip[35,46]. In these experiments, we were able to visualize time-dependent changes of the local potential distribution caused by the surface corrosion even when the surface structure does not show any changes. This confirms that the influence of the cross talk is negligible compared to the contribution form the actual local potential distribution.

The local surface potential image (Figure 8d) shows that most of the surface is negatively charged compared to the bulk solution, indicating a relatively low corrosion activity of the imaged area. This is more clearly observed in the Z cross section taken from the 3D potential map as shown in Figure 8(g). While the potential contrasts at far from the surface are caused by noise, the contrasts near the surface represents the local potential induced by the charges accumulated in the EDL. This image shows that the negative charges are accumulated on most of the areas except for the very limited spots. In addition, the Z profiles show that the SR potential change takes place only within 30 nm from the surface. This is almost 10 times smaller than that observed in Figures 6

and 7 in spite of the same solution condition (i.e. 0.1 mM NaCl solution). This result suggests that the effective local C_{ion} near the surface was 100 times higher than expected. In this study, we performed experiments with an open liquid cell, where solvent can slowly evaporate during the experiment. The 2D and 3D images were taken after 2 h since we immersed the sample into the solution. Therefore, it is likely that the effective C_{ion} was significantly enhanced due to the dissolution of Cu and the evaporation of water by the time we started the imaging. These discussions on the polarity, magnitude and vertical extent of the interfacial potential were impossible before 3D-OL-EPM becomes available. This is a great advancement from 2D-OL-EPM, where we can only visualize a lateral distribution of relative potential values.

At this stage, there are some practical limitations in the performance and applicability of the proposed method. As we previously reported for the 2D-OL-EPM, the maximum concentration of the electrolyte is still limited to less than 10 mM[31]. While we can use not only metals but also oxides as a sample, they should have a sufficient electrical conductivity. As we can see in Figure 8, the quality of the local surface potential image obtained by 3D-OL-EPM is not as good as that of the 2D-OL-EPM image. This is not only because of the low pixel resolution but also because of the noise. In the LR subtraction process, a linear fit curve is extrapolated to estimate the contribution at the zero distance (see Figure 3c). Thus, even a slight error in the estimated slope caused by the noise can result in a large potential error at the zero distance. However, there still remains a large room for the improvements in the force resolution, imaging speed and scanning method in the current 3D-OL-EPM. Therefore, it is highly likely that these issues will be solved by further technical developments in the future.

4 Conclusions

In this study, we have investigated the possibility of visualizing charges accumulated at an electrode-electrolyte interface by OL-EPM. We discussed the contributions of the force components having different timescales and interaction ranges to the errors in OL-EPM measurements. In particular, we pointed out the significant contribution of the LR force to the errors. Based on this understanding, we proposed practical ways to reduce these errors. For 2D potential imaging, we proposed to use Equation (9) or (10). For Z potential spectroscopy, we proposed to subtract the linear part of the Z potential profile from its original.

With these two improvements, we measured Z potential profiles with varying E on a polarizable and non-polarizable electrode. The opposite charge accumulation behaviors of these two types of electrodes were successfully visualized, which confirmed the capability of OL-EPM to visualize charges accumulated at an electrode-electrolyte interface. The results also showed that the OL-EPM potential after the LR subtraction represents relative values with respect to the bulk solution potential. This is significant progress from the 2D-OL-EPM imaging, where the zero potential does not have a specific meaning.

To take advantage of this capability, we performed 3D-OL-EPM measurements of Cu fine wires and compared the results with those obtained by 2D-OL-EPM. The results show that the magnitude of the lateral potential variations is similar for both the methods although the absolute values are different. This confirms that 2D-OL-EPM is still useful for visualizing lateral potential distributions with a high pixel density and a fast imaging speed. The results also demonstrated that the comparison between the Z cross section of the 3D potential map and the E dependence of the Z potential profile provides valuable insights into the electrochemical reactions and the local solution conditions at the solid-liquid interface. Such real-space information on the charge distributions in an EDL is critically important in various academic and industrial research on electronics devices, electrochemistry, tribology and life sciences.

Acknowledgements

This work was supported by ACT-C, Japan Science and Technology Agency and World Premier International Research Center Initiative (WPI), MEXT, Japan.

Notes and references

1 B. B. Damaskin and A. N. Frumkin, *Electrochim. Acta*, 1974, **19**, 173–176.
2 J.-J. Velasco-Velez, C. H. Wu, T. A. Pascal, L. F. Wan, J. Guo, D. Prendergast and M. Salmeron, *Science*, 2014, **346**, 831–834.
3 H. Greberg and R. Kjellander, *J. Chem. Phys.*, 1998, **108**, 2940–2953.
4 Q. Ji, X. An, H. Liu, L. Guo and J. Qu, *ACS Nano*, 2015, **9**, 10922–10930.
5 R. Vangara, F. van Swol and D. N. Petsev, *J. Chem. Phys.*, 2017, **147**, 214704.
6 S. T. Martin, J. M. Kesselman, D. S. Park, N. S. Lewis and M. R. Hoffmann, *Environ. Sci. Technol.*, 1996, **30**, 2535–2542.
7 S. Martinez and M. Metikoš-Huković, *J. Appl. Electrochem.*, 2003, **33**, 1137–1142.
8 W. Xing, S. Z. Qiao, R. G. Ding, F. Li, G. Q. Lu, Z. F. Yan and H. M. Cheng, *Carbon*, 2006, **44**, 216–224.
9 C. Largeot, C. Portet, J. Chmiola, P.-L. Taberna, Y. Gogotsi and P. Simon, *J. Am. Chem. Soc.*, 2008, **130**, 2730–2731.
10 K. Urita, N. Ide, K. Isobe, H. Furukawa and I. Moriguchi, *ACS Nano*, 2014, **8**, 3614–3619.
11 D. Kang, Q. Liu, J. Gu, Y. Su, W. Zhang and D. Zhang.
12 H. Yuan, H. Shimotani, A. Tsukazaki, A. Ohtomo, M. Kawasaki and Y. Iwasa, *Adv. Funct. Mater.*, 2009, **19**, 1046–1053.
13 T. A. Petach, K. V. Reich, X. Zhang, K. Watanabe, T. Taniguchi, B. I. Shklovskii and D. Goldhaber-Gordon, *ACS Nano*, 2017, **11**, 8395–8400.
14 M. Suda, R. Kato and H. M. Yamamoto, *Science*, 2015, **347**, 743–746.
15 Y. Yamada, K. Ueno, T. Fukumura, H. T. Yuan, H. Shimotani, Y. Iwasa, L. Gu, S. Tsukimoto, Y. Ikuhara and M. Kawasaki, *Science*, 2011, **332**, 1065–1067.
16 M. Lashkari and M. R. Arshadi, *Chem. Phys.*, 2004, **299**, 131–137.
17 J. Israelachvili and H. Wennerström, *Nature*, 1996, **379**, 219–

225.
18 A. T. Poortinga, R. Bos, W. Norde and H. J. Busscher, *Surf. Sci. Rep.*, 2002, **47**, 1–32.
19 P. Attard, *Adv. Chem. Phys.*, 1996, **92**, 1–159.
20 J.-P. Hansen and H. Löwen, *Annu. Rev. Phys. Chem.*, 2000, **51**, 209–242.
21 L. Fan, Y. Liu, J. Xiong, H. S. White and S. Chen, *ACS Nano*, 2014, **10**, 10426–10436.
22 I. Chowdhury, M. C. Duch, N. D. Mansukhani, M. C. Hersam and D. Bouchard, *Environ. Sci. Technol.*, 2013, **47**, 6288–6296.
23 G. Binnig, C. F. Quate and C. Gerber, *Phys. Rev. Lett.*, 1986, **56**, 930.
24 K.-I. Umeda, K. Kobayashi, N. Oyabu, K. Matsushige and H. Yamada, *Nanotechnology*, 2015, **26**, 285103.
25 C. Zhao, D. Ebeling, I. Siretanu, D. van den Ende and F. Mugele, *Nanoscale*, 2015, **7**, 16298–16311.
26 M. Nonnenmacher, M. P. O'Boyle and H. K. Wickramasinghe, *Appl. Phys. Lett.*, 1991, **58**, 2921–2923.
27 N. Kobayashi, H. Asakawa and T. Fukuma, *Rev. Sci. Instrum.*, 2010, **81**, 123705.
28 L. Collins, S. Jesse, J. I. Kilpatrick, A. Tselev, O. Varenyk, M. B. Okatan, S. A. L. Weber, A. Kumar, N. Balke, S. V. Kalinin and B. J. Rodriguez, *Nat. Comm.*, 2014, **5**, 38971.
29 K.-I. Umeda, N. Oyabu, K. Kobayashi, Y. Hirata, K. Matsushige and H. Yamada, *Appl. Phys. Express*, 2010, **3**, 065205.
30 N. Kobayashi, H. Asakawa and T. Fukuma, *J. Appl. Phys.*, 2011, **110**, 044315.
31 N. Kobayashi, H. Asakawa and T. Fukuma, *Rev. Sci. Instrum.*, 2012, **83**, 033709.
32 K.-I. Umeda, K. Kobayashi, N. Oyabu, Y. Hirata, K. Matsushige and H. Yamada, *J. Appl. Phys.*, 2013, **113**, 154311.
33 K.-I. Umeda, K. Kobayashi, N. Oyabu, Y. Hirata, K. Matsushige and H. Yamada, *J. Appl. Phys.*, 2014, **116**, 134307.
34 L. Collins, J. I. Kilpatrick, S. A. L. Weber, A. Tselev, I. V. Vlassiouk, I. N. Ivanov, S. Jesse, S. V. Kalinin and B. J. Rodriguez, *Nanotechnology*, 2013, **24**, 475702.
35 K. Honbo, S. Ogata, T. Kitagawa, T. Okamoto, N. Kobayashi, I. Sugimoto, S. Shima, A. Fukunaga, C. Takatoh and T. Fukuma, *ACS Nano*, 2016, **10**, 2575–2583.
36 T. Fukuma, M. Kimura, K. Kobayashi, K. Matsushige and H. Yamada, *Rev. Sci. Instrum.*, 2005, **76**, 053704.
37 T. Fukuma and S. P. Jarvis, *Rev. Sci. Instrum.*, 2006, **77**, 043701.
38 T. Fukuma, *Rev. Sci. Instrum.*, 2009, **80**, 023707.
39 T. Fukuma, K. Onishi, N. Kobayashi, A. Matsuki and H. Asakawa, *Nanotechnology*, 2012, **23**, 135706.
40 W. A. Ducher, T. J. Senden and R. M. Pashley, *Langmuir*, 1992, **81**, 1831.
41 S. Biggs and P. Mulvaney, *J. Chem. Phys.*, 1994, **100**, 8501.
42 K. Hu and A. J. Bard, *Langmuir*, 1997, **13**, 5114.
43 T. Ederth, *J. Phys. Chem. B*, 2000, **104**, 9704.
44 M. Giesbers, J. M. Kleijn and M. A. C. Stuart, *J. Colloid. Interface Sci.*, 2002, **248**, 88–95.
45 D. Barten, J. M.Kleijn, J. Duval, H. P. v. Leeuwen, J. Lyklema and M. A. C. Stuart, *Langmuir*, 2003, **19**, 1133.
46 S. Ogata, N. Kobayashi, T. Kitagawa, S. Shima, A. Fukunaga, C. Takatoh and T. Fukuma, *Corros. Sci.*, 2016, **105**, 177–182.

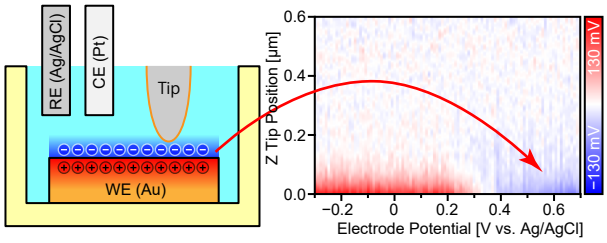

TOC Figure:

Charge accumulation behavior at the Au-electrolyte interface was visualized by three-dimensional open-loop electric potential microscopy with varying electrode potential.